

Article

The Preparation of Amorphous Aluminum Oxide Modified g-C₃N₄ to Improve Photocatalytic Performance in Contaminant Degradation Applications

Yining Zheng, Congcong Wang, Wenjing Fu, Qi An, Cundi Wei and Lina Li *

Key Laboratory of Automobile Materials of Ministry of Education, Solid Waste Recycling Engineering Research Center of Jilin, School of Materials Science and Engineering, State Key laboratory of Inorganic Synthesis & Preparative Chemistry, Jilin University, Changchun 130022, China; zhengyn.1007@foxmail.com (Y.Z.); congcong18@mails.jlu.edu.cn (C.W.); fuwjij@foxmail.com (W.F.); anqi18@mails.jlu.edu.cn (Q.A.); weicd@jlu.edu.cn (C.W.)

* Correspondence: lilina@jlu.edu.cn; Tel.: +86-138-4406-7649

Received: 5 August 2020; Accepted: 3 September 2020; Published: 9 September 2020



Abstract: For the first time, aluminum alloy was used as the main source to prepare aluminum oxide-modified carbon nitride with a melamine–cyanuric acid supramolecular complex. The introduction of amorphous aluminum oxide confers macroporosity to the skeletons of g-C₃N₄-AlO_x. Its surface area increased to 75.5 m²g⁻¹, about 1.5 times that of single g-C₃N₄. After modification, the visible light response range was expanded, especially at 450–500 nm, while the band structure could be adjusted. Compared with g-C₃N₄, g-C₃N₄-AlO_x has better photocatalytic performance, the adsorption rate for the dye rhodamine B (RhB) is about 2.1 times that of g-C₃N₄, and the RhB removal rate is 1.2 times that of g-C₃N₄.

Keywords: g-C₃N₄; modification; aluminum alloy as aluminum source; photocatalysis; porosity introduction

1. Introduction

The rapid development of global industrialization and growth of population have led to increasing demand for energy. With non-renewable energy sources being increasingly consumed and rapidly depleted, the effective utilization and development of renewable energy sources has become extremely urgent and received wide attention [1–3].

As an important part of renewable energy, solar energy has competitive advantages, such as wide distribution, large energy reserves, cleanliness and safety [3,4]. In order to promote the usage of solar energy, research on photocatalytic materials with good stability and high activity becomes a key topic in material science [5–9]. Among all the materials, g-C₃N₄ is eye-catching because of its low cost, low toxicity and wide light response range [10–12]. Since the first report about its use in water splitting in 2009 [13], related reports have continued. Compared with the classic photocatalyst TiO₂, g-C₃N₄ not only exhibits satisfying photocatalytic activity under ultraviolet light but also can be activated by part-visible light [5,14–16]. This property makes g-C₃N₄ appealing, as visible light accounts for about 43% of the solar spectrum [4,17,18]. To date, its application in photocatalysis includes water splitting [13,19], organic matter degradation [20,21], CO₂ reduction [22–24] and photocatalytic organic reactions [24,25].

However, g-C₃N₄ still presents several disadvantages, such as its low specific surface area, low charge mobility, high excitation dissociation energy, high electron hole recombination rate and

inappropriate valence electron positions [19,26–28]. These limitations result in the low quantum efficiency of g-C₃N₄ at an irradiation wavelength of 420–460 nm [13,29]. A lot of research on g-C₃N₄ modification has been carried out to improve its catalytic efficiency, including acid treatment [30], noble metal deposition [31,32], anchoring dye sensitization [33], morphological modification [34,35], etc. In addition, doping is also an effective way to introduce impurities into the g-C₃N₄ matrix to change the electronic structure and energy band configuration, such as non-metallic element doping and metal oxide semiconductor coupling with g-C₃N₄ to form heterojunctions (Cu₂O, TiO₂, ZnO, etc.) [6,36–39]. In fact, the formation of a heterojunction between metal oxide and g-C₃N₄ can effectively shorten the distance of the electron transport path, inhibit the rapid recombination of photo-generated electron holes and provide more sites for g-C₃N₄ to bind to the reaction substrate in the photocatalytic process [40].

Al₂O₃, as a cheap, non-toxic material, can combine with g-C₃N₄ to enhance the photocatalytic activity of g-C₃N₄. Compared with other metal oxides, aluminum oxide has the advantages of abundant reserves, a low cost, no pollution, good chemical inertia, good thermal stability, a large specific surface area and so on [4]. Its photoelectron defects can effectively inhibit the fast recombination of photoexcited carriers in Al₂O₃/g-C₃N₄ material, so the material has better photocatalytic activity. Previous studies have reported that although alumina does not have photocatalytic activity, amorphous alumina indeed helped with Al₂O₃/g-C₃N₄'s photocatalytic performance. That is owing to the defect sites of Al₂O₃, which can accept electrons from g-C₃N₄ in the Al₂O₃/g-C₃N₄ composite and inhibit the fast recombination of photoexcited carriers [4,41]. Currently, effective coupling methods include ultrasonic dispersion, chemical adsorption, in situ thermal polymerization and so on. [20] In order to achieve better performance, new strategies for preparation should be explored to expand the possible material scope. Herein, a better preparation method that can combine aluminum oxide with g-C₃N₄ is explored. In this protocol, aluminum alloy was directly used as an Al source to form g-C₃N₄-AlO_x with melamine (M) and cyanic acid (CA). Using this method, g-C₃N₄-AlO_x was well mixed with a homogeneous element distribution, and its specific surface area was about 1.5 times that of g-C₃N₄. The photocatalytic performance of g-C₃N₄-AlO_x was significantly improved compared with that of g-C₃N₄ in rhodamine B (RhB) degradation experiments.

2. Result and Discussion

2.1. Characterization of As-Prepared Samples

X-ray diffraction was used in order to reveal the structure and crystallinity variation of materials before and after the calcination process. As shown in Figure 1a, under the condition of continuous stirring, cyanuric acid and melamine would form a cyanuric acid–melamine (CM) supramolecular complex with a characteristic peak at around 27.9°. The AlO_xH_y colloid prepared in this protocol shows no specific XRD patterns, revealing its amorphous nature. With the addition of AlO_xH_y colloids, the main peaks of CM-AlO_xH_y remained similar to those of CM, illustrating that the main skeleton of the composite was still CM. The intensity of these peaks decreased compared with those of the CM complex, which shows the successful introduction of the AlO_xH_y colloid. After calcination, it could be found that the CM turned to g-C₃N₄, with a specific peak at 27.4°, representing its two dimensional structure. The XRD pattern of g-C₃N₄-AlO_x is basically consistent with that of single g-C₃N₄, suggesting that the main composition of g-C₃N₄-AlO_x is g-C₃N₄. The characteristic peak at 27.3° is marked as g-C₃N₄ (JCPDS #87-1526), and the (002) plane of the aromatic segment is stacked between the planes [42,43]. The refined lattice parameters of g-C₃N₄ and composite material g-C₃N₄-AlO_x obtained by using the Scherrer formula [44,45] are $a = 398$ (340) Å and $a = 52$ (5) Å, respectively. This shows that compounding the materials can effectively reduce the grain size of g-C₃N₄.

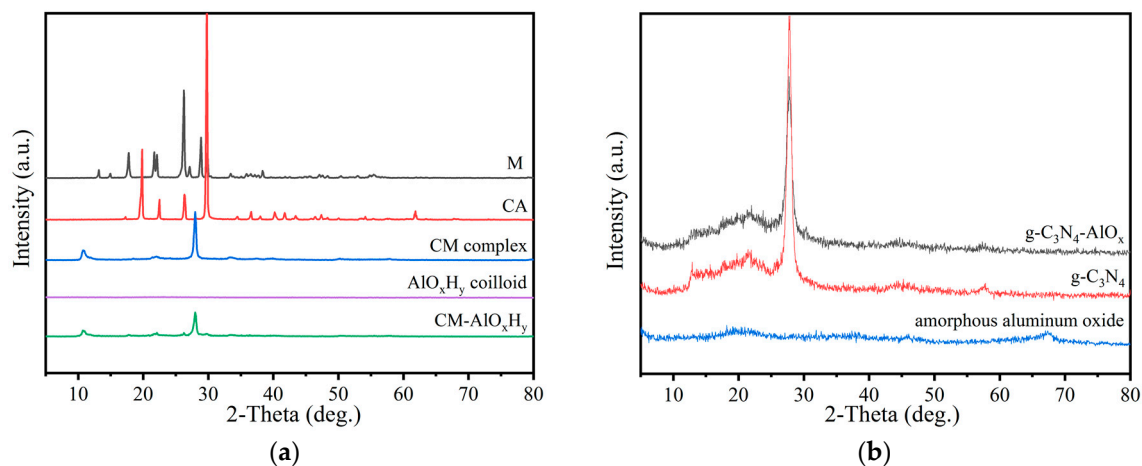


Figure 1. XRD patterns of single g-C₃N₄, g-C₃N₄-AlO_x and amorphous aluminum oxide before (a) and after calcination (b).

The surface area, porosity of g-C₃N₄, composite g-C₃N₄-AlO_x and amorphous aluminum oxide were studied with the nitrogen adsorption–desorption method at 77 K. All samples were treated under vacuum at 423 K for 4 h prior to these measurements. It can be observed from Figure 2a that the N₂ adsorption isotherms of g-C₃N₄, g-C₃N₄-AlO_x and amorphous aluminum oxide increase slowly at low relative pressure and sharply at high relative pressure. These materials present type IV isotherms with hysteresis loops of type 3 (H3), revealing the samples are all mesoporous materials. Based on this information, the specific surface areas were calculated with the BET model. The BET surface area of g-C₃N₄, g-C₃N₄-AlO_x and amorphous aluminum oxide were evaluated to be 51.1, 75.5 and 189.2 m²g^{−1}, respectively. The surface area of g-C₃N₄-AlO_x was higher than that of g-C₃N₄, which would be helpful in catalysis. Its surface area is between that of g-C₃N₄ and that of amorphous aluminum oxide, suggesting the successful combination of the two components in the new material. The pore size distributions of the samples were calculated with the Nonlocal Density Functional Theory (NLDFT) method, as shown in Figure 2b. Compared with that of g-C₃N₄ and amorphous aluminum oxide, the porosity of g-C₃N₄-AlO_x includes not only the mesoporous part but also macroporosity (60–130 nm). The appearance of new porosity displays a new structure in g-C₃N₄-AlO_x, which means that the CM complex and AlO_xH_y colloid are not simply mixed together in the g-C₃N₄-AlO_x but they form new material. This proves that the new preparation strategy is valuable for achieving new materials and expanding the material scope. Additionally, the material in this method very likely possesses a heterojunction structure, which is usually preferred in semiconductor catalysis.

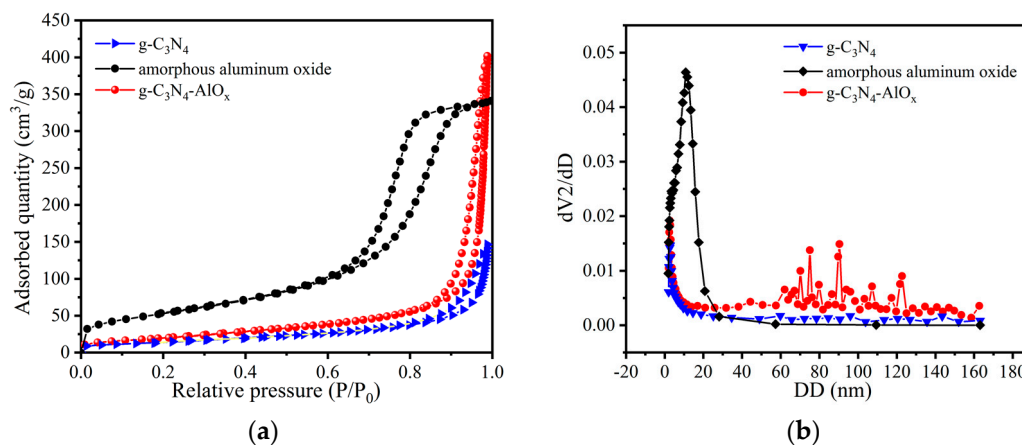


Figure 2. (a) N₂ adsorption–desorption isotherm, and (b) pore size distribution diagram of single g-C₃N₄, g-C₃N₄-AlO_x and amorphous aluminum oxide.

The morphology of $g\text{-C}_3\text{N}_4\text{-AlO}_x$ was investigated with SEM as shown in Figure 3. The SEM photos show that single $g\text{-C}_3\text{N}_4$ displays tubular structures, with a diameter of about 500 nm, and a relatively smooth surface (Figure 3a). For amorphous aluminum oxide-decorated $g\text{-C}_3\text{N}_4$, the morphology changes greatly into an irregular “coralloid” structure with a rough surface (Figure 3b,c). Importantly, a large number of pores appear in the “coralloid” structure, whose existence is consistent with the results of the N_2 adsorption–desorption measurements discussed above. The morphology variation intuitively proves the change in material structure and influence of Al colloids. In order to reveal the element composition, $g\text{-C}_3\text{N}_4\text{-AlO}_x$ was analyzed with energy dispersive X-ray energy spectroscopy (EDS). The EDS mapping images (Figure 3d) suggest that the four main elements Al, C, N and O are extensively distributed in $g\text{-C}_3\text{N}_4\text{-AlO}_x$. This even existence of amorphous aluminum oxide is probably the reason for the increased in surface area, in that they act as template agents during the skeleton formation process. It also shows that the method of mixing AlO_xH_y colloid with supramolecular complex CM is so effective that the amorphous alumina keeps close contact with $g\text{-C}_3\text{N}_4$. The close combination of two materials provides the possibility of a heterojunction structure, which may be good for further catalysis applications. The selected area in Figure 3b was analyzed, and the corresponding EDX results are given in Table 1. The EDX results reveal that the amorphous aluminum oxide makes up about 5.10 wt% of $g\text{-C}_3\text{N}_4\text{-AlO}_x$ (here, X is defaulted to 1.5).

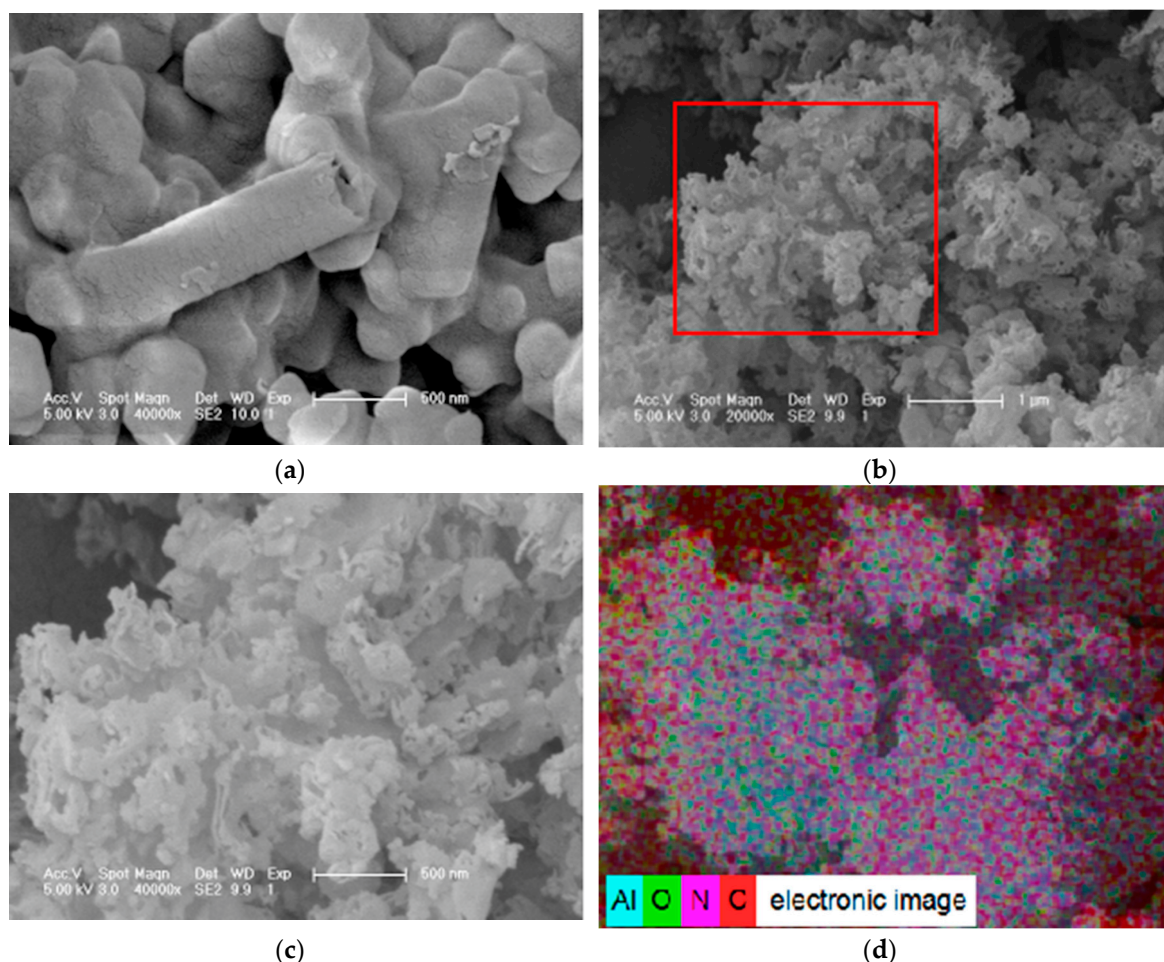
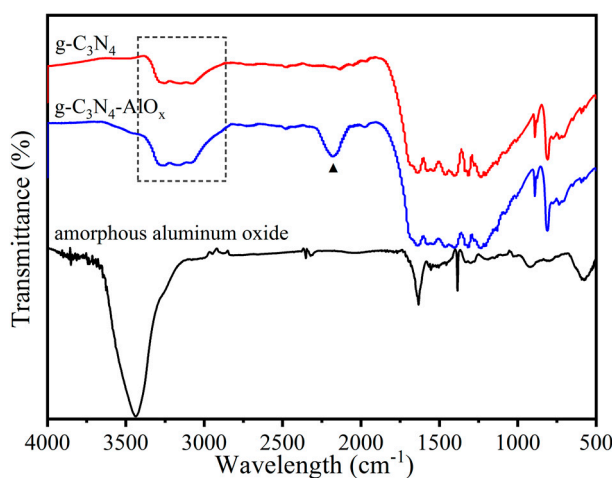


Figure 3. SEM images of (a) single $g\text{-C}_3\text{N}_4$; (b and c) $g\text{-C}_3\text{N}_4\text{-AlO}_x$; and (d) energy-dispersive X-ray (EDX) mapping of $g\text{-C}_3\text{N}_4\text{-AlO}_x$.

Table 1. The element content distribution according to EDS mapping analysis of g-C₃N₄-AlO_x for a selected area.

Element	Weight%	Atomic%
C	39.61	44.19
N	51.52	49.30
Al	2.68	1.33

The samples were characterized by Fourier transform infrared spectroscopy (FTIR), as shown in Figure 4. g-C₃N₄-AlO_x possesses the peaks most characteristic of g-C₃N₄ in the FTIR spectrum. This shows that its main structure is similar to that of g-C₃N₄, which is a connected heptazine ring. The peak band around 3000–3450 cm⁻¹ is attributed to the stretching vibration of N-H and hydroxyl (O-H) groups, and is derived from the process of supramolecular dehydration while forming g-C₃N₄. Compared with the peak band in the box of g-C₃N₄, the peak band of g-C₃N₄-AlO_x near 3000–3450 cm⁻¹ is broadened and the peak strength is slightly increased, indicating that there were more hydroxyl groups on the surface of g-C₃N₄-AlO_x. This is possibly because AlO_xH_y colloid joins the supramolecular formation and changes the surface structure of the original g-C₃N₄. It is worth noting that g-C₃N₄-AlO_x has an absorption peak near 2200 cm⁻¹, which is not shown in the graphs of single g-C₃N₄ and amorphous aluminum oxide. This absorption peak is attributed to the peak characteristic of C≡N. The appearance of this new peak again illustrates that AlO_xH_y colloid affects the supramolecular formation and, later, the g-C₃N₄-AlO_x synthesis. In the presence of AlO_xH_y, some triazine rings in the supramolecular formation do not condense into heptazine rings completely but result in C≡N on the surface of the material. Overall, this is consistent with the previous analysis showing that g-C₃N₄-AlO_x is a new material from g-C₃N₄ surface decoration.

**Figure 4.** FTIR absorption spectra of single g-C₃N₄, g-C₃N₄-AlO_x and amorphous aluminum oxide.

The details of g-C₃N₄-AlO_x regarding the chemical composition and local connectivity motifs were revealed by X-ray photoelectron spectroscopy (XPS, Figure 5). In the C1s curve of single g-C₃N₄, the main signal peak appears at 288.3 eV, which is attributed to sp²C in triazine rings (N-C=N₂). (The other peak around 284.8 eV is recognized as adventitious carbon from impurities.) After the decoration of AlO_x colloids, the C1s peak in g-C₃N₄-AlO_x becomes shifted to a higher binding energy area (288.4 eV), indicating its chemical environment has changed and there is close interaction between amorphous aluminum oxide and g-C₃N₄ (Figure 5a). The N1s spectrum of g-C₃N₄-AlO_x was similar to that of g-C₃N₄, which shows that the main framework of g-C₃N₄-AlO_x is still g-C₃N₄ (Figure 5b). Compared with those for amorphous aluminum oxide, the positions of the O1s peak and Al2p peak also exhibit variation in g-C₃N₄-AlO_x. In amorphous aluminum oxide, the positions of O1s and Al2p locate at 531.3 and 74.4 eV, which are shifted to 532.1 and 74.7 eV in g-C₃N₄-AlO_x (Figure 5b,c).

This change illustrates strong chemical interaction between the two components, which suggests the successful preparation of $g\text{-C}_3\text{N}_4\text{-AlO}_x$ with an interactive interface.

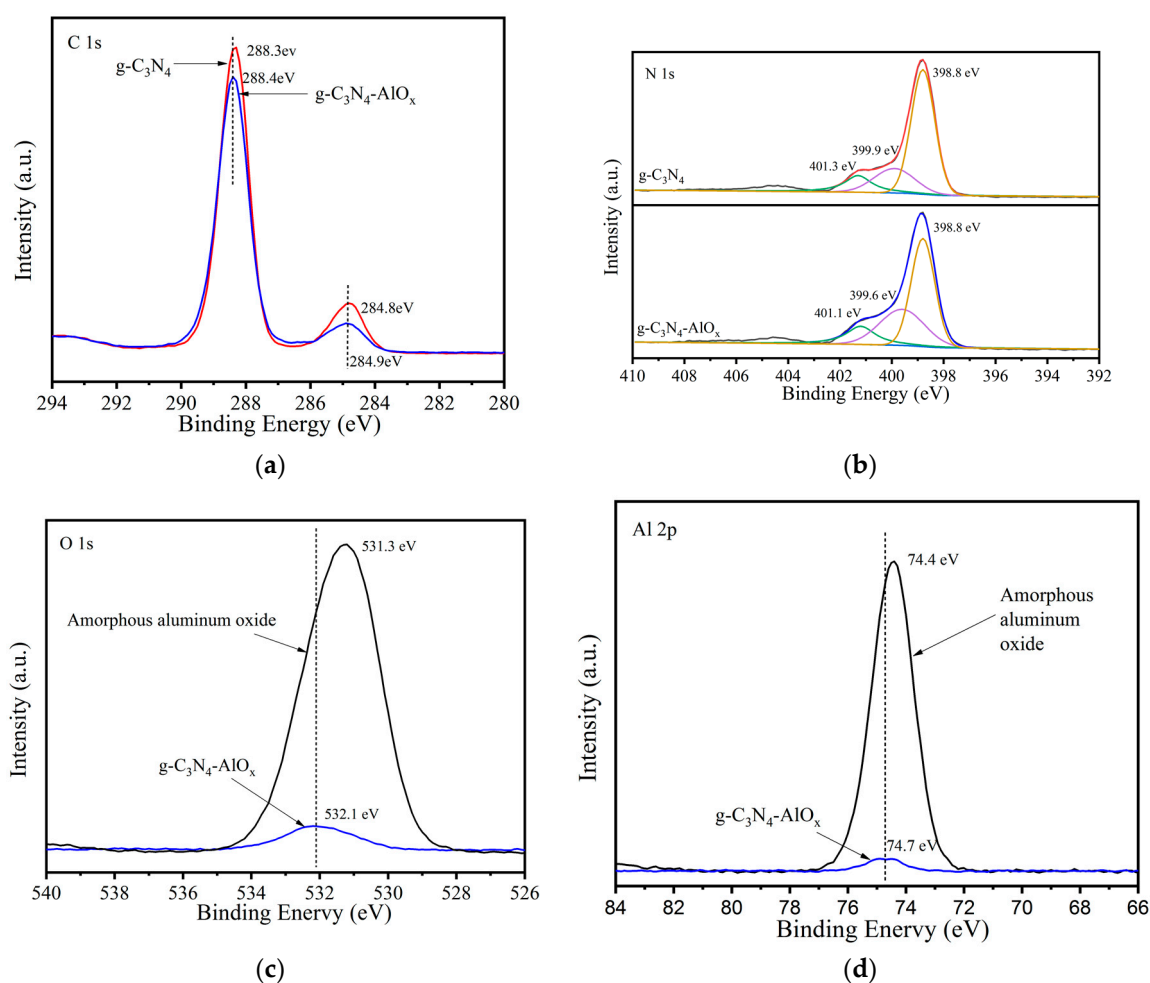


Figure 5. High resolution XPS spectra of the (a) C1s, (b) N1s, (c) O1s and (d) Al2p peaks of the samples.

The $g\text{-C}_3\text{N}_4$, $g\text{-C}_3\text{N}_4\text{-AlO}_x$ and amorphous aluminum oxide were studied with solid UV-vis absorption spectroscopy. As shown in Figure 6a, pristine $g\text{-C}_3\text{N}_4$ exhibits a light absorption range from ultraviolet light to visible light, and its absorption edge wavelength is at around 450 nm. After decoration with AlO_xH_y colloid, the absorption edge of $g\text{-C}_3\text{N}_4\text{-AlO}_x$ was redshifted to around 500 nm, which is an improvement for wider solar light spectrum absorption. The redshift of adsorption usually comes from the enlargement of conjugations. Here, the variation of adsorption may imply that amorphous aluminum oxide takes part in the conjugations in the new system. In the $g\text{-C}_3\text{N}_4\text{-AlO}_x$, the conjugation may contain $p\text{-}\pi$ conjugation, instead of only $\pi\text{-}\pi$ conjugation from $g\text{-C}_3\text{N}_4$. As amorphous aluminum oxide only responds to ultraviolet light, the better light response performance of $g\text{-C}_3\text{N}_4\text{-AlO}_x$ is indeed due to the decoration effect of aluminum oxide on $g\text{-C}_3\text{N}_4$, instead of simple mixing. The band gap of those materials can be calculated with the Tauc plot method. The bandgap of $g\text{-C}_3\text{N}_4\text{-AlO}_x$ is calculated to be 2.51 eV, which is a little narrower than that of $g\text{-C}_3\text{N}_4$, at around 2.66 eV. One possible reason for this result is that the addition of AlO_xH_y colloid leads to lower crystallinity (Figure 1b) and more crystal defects in $g\text{-C}_3\text{N}_4\text{-AlO}_x$. In addition, in Figure 6, it is also clear that $g\text{-C}_3\text{N}_4\text{-AlO}_x$ has two components in its absorbance edge, which implies that the sample is not monodisperse in size. In this protocol, amorphous aluminum oxide was successfully doped but probably not evenly dispersed. To further determine the valence band level, $g\text{-C}_3\text{N}_4\text{-AlO}_x$ samples were characterized by ultraviolet photoelectron spectroscopy (UPS, Figure 6c). The maximum values of the $g\text{-C}_3\text{N}_4$ and

$g\text{-C}_3\text{N}_4\text{-AlO}_x$ valence bands were -5.96 and -5.36 eV vs. vacuum or 1.46 and 0.86 eV vs. NHE (Normal Hydrogen Electrode); E (eV) = $-4.5 - E_{\text{NHE}}$ (V) [37]. Considering the width of the forbidden band, the minimum values of the corresponding conduction band are calculated to be -1.20 and -1.65 V vs. NHE, respectively. This result proves this method is effective in band structure adjustment, which provides $g\text{-C}_3\text{N}_4\text{-AlO}_x$ with completely different possibilities in photocatalysis.

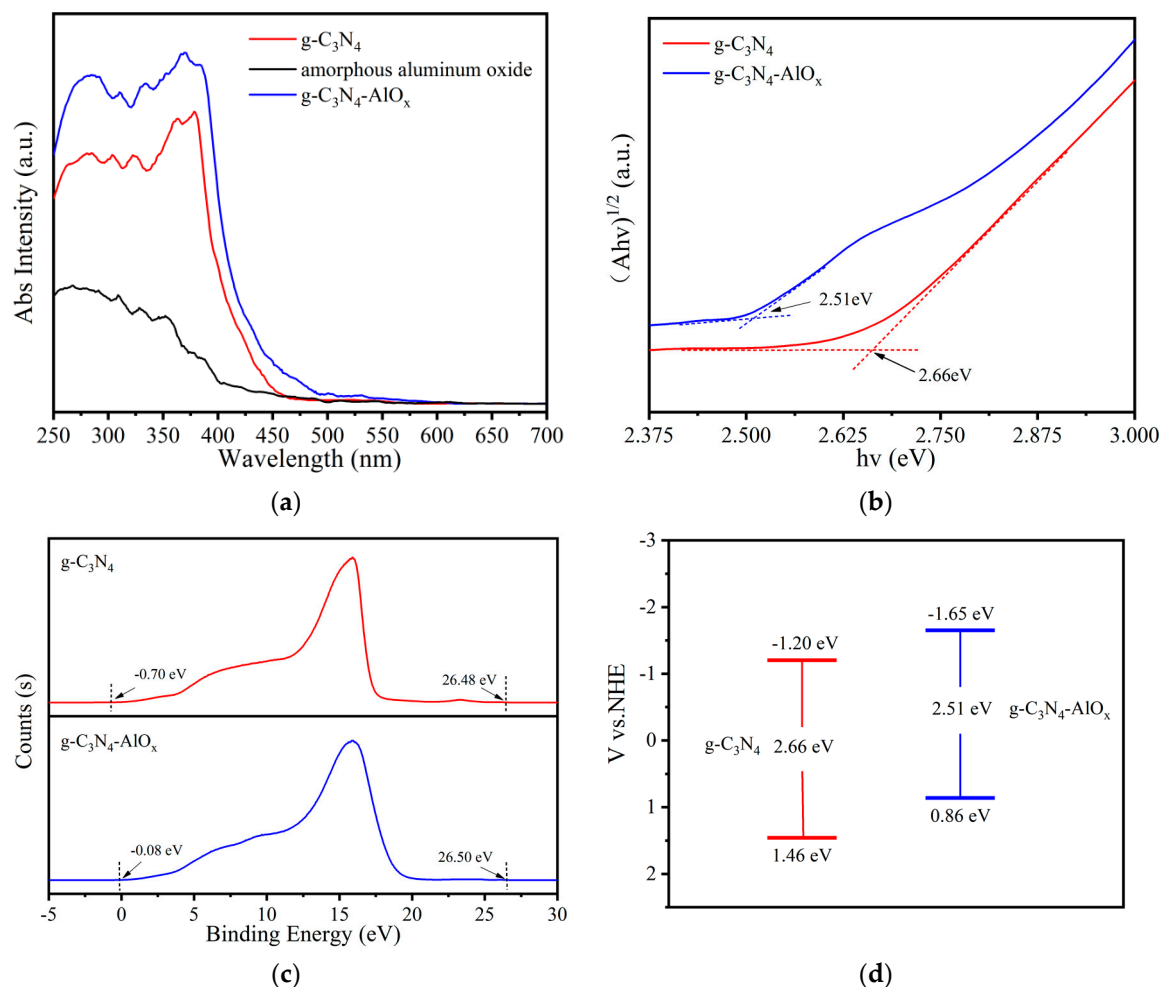


Figure 6. (a) UV-vis absorption spectra, (b) Tauc's plot, (c) ultraviolet photoelectron spectra (UPS) and (d) band structures of single $g\text{-C}_3\text{N}_4$, $g\text{-C}_3\text{N}_4\text{-AlO}_x$ and amorphous aluminum oxide.

2.2. Photocatalytic Activity

The photocatalytic activity of $g\text{-C}_3\text{N}_4\text{-AlO}_x$ was investigated with a rhodamine B (RhB) degradation experiment under visible light irradiation. In a typical degradation test, 5.0 mg of powder was added as a catalyst in 10.0 mL of RhB aqueous solution (10 mgL^{-1}). After 30 mins of stirring in the dark, the whole system was subjected to white light illumination (380–840 nm). During the whole degradation process, the remaining RhB concentration was tested every 20 min by obtaining UV-vis spectra at the wavelength of 554 nm as shown in Figure 7. Amorphous aluminum oxide can absorb a small amount of dyes in the dark but can hardly degrade dyes in visible light. $g\text{-C}_3\text{N}_4\text{-AlO}_x$ displays better photocatalytic performance than $g\text{-C}_3\text{N}_4$, successfully eliminating 92.77% of the RhB within 80 min (Figure 7a). For better intuitiveness, the RhB degradation performance of $g\text{-C}_3\text{N}_4\text{-AlO}_x$ and single $g\text{-C}_3\text{N}_4$ is compared in terms of photodegradation first order profiles in Figure 7b. Those curves are in good agreement with the pseudo-first-order correlation of kinetics:

$$\ln(C_0/C_t) = kt + \ln(C_0/C_1), \quad (1)$$

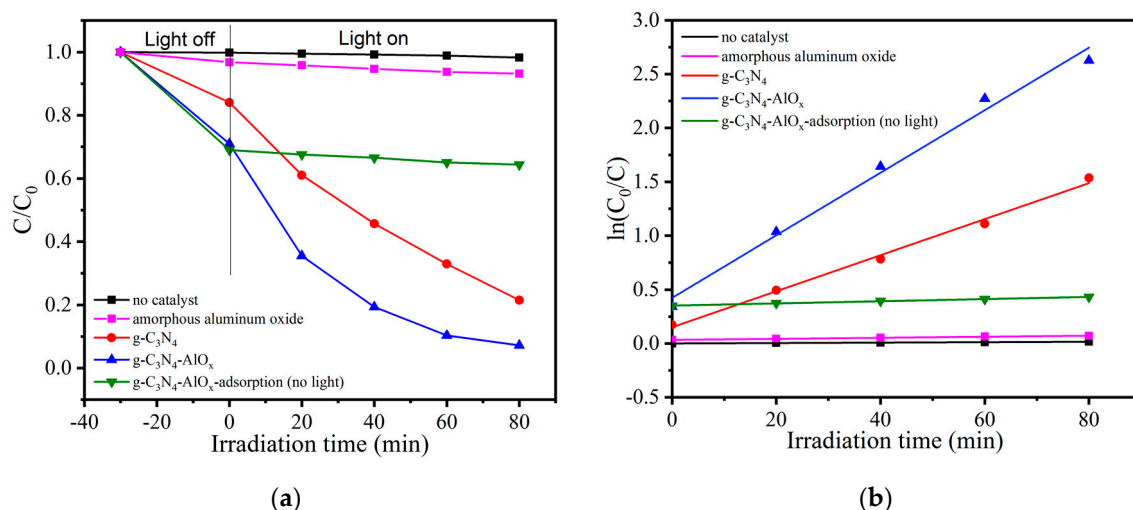


Figure 7. (a) Photocatalytic activity comparison for rhodamine B (RhB) photodegradation by the samples under visible light irradiation, and (b) first order profiles of photodegradation of RhB by the samples.

C_0 : initial concentration of the dye; C_t : instantaneous concentration of the dye; C_1 : the dye concentration after 30 min of adsorption; $\ln(C_0/C_1)$: the adsorption efficiency of the photocatalyst for RhB; $\ln(C_0/C)$: the degradation efficiency of the photocatalyst for RhB.

The calculated pseudo-first-order rate constant K and correlation coefficient R are shown in Table 2. According to the value of the intercept $\ln(C_0/C_1)$ on the vertical axis of the dynamic curve, it can be found that the adsorption rate of $g-C_3N_4-AlO_x$ for RhB is about 2.1 times higher than that of $g-C_3N_4$ for RhB. This reveals that the amorphous aluminum oxide indeed helps with the promotion of photocatalytic performance. Amorphous aluminum oxide provides more sites for $g-C_3N_4$ electrons to combine, promotes electron-hole separation and improves photocatalytic activity. Besides, $g-C_3N_4-AlO_x$ possesses a large number of macroporous structures, in which incident light is more prone to multiple scattering, increasing the light utilization rate of the material. The doping of amorphous alumina confers a smaller grain size and larger porosity to the final composite material.

Table 2. Kinetic fitting equation, quasi-first-order rate constant k and correlation coefficient in the process of the degradation of RhB by each sample prepared.

Sample	Fitted Equation	k (min^{-1})	Correlation Coefficient R
no catalyst	$\ln(C_0/C_t) = 1.96 \times 10^{-4}t + 3.37 \times 10^{-4}$	1.96×10^{-4}	9.89×10^{-1}
$g-C_3N_4$	$\ln(C_0/C_t) = 1.42 \times 10^{-2}t - 5.39 \times 10^{-2}$	1.42×10^{-2}	9.94×10^{-1}
$g-C_3N_4-AlO_x$	$\ln(C_0/C_t) = 2.92 \times 10^{-2}t - 1.10 \times 10^{-1}$	2.92×10^{-2}	9.94×10^{-1}
$g-C_3N_4-AlO_x$ -adsorption	$\ln(C_0/C_t) = 1.01 \times 10^{-3}t + 3.52 \times 10^{-1}$	1.01×10^{-3}	9.97×10^{-1}
amorphous aluminum oxide	$\ln(C_0/C_t) = 4.89 \times 10^{-4}t + 3.34 \times 10^{-2}$	4.89×10^{-4}	9.92×10^{-1}

3. Materials and Methods

3.1. Materials

Al-Ga-In ternary alloy (99% aluminum), melamine ($C_3N_3(NH_2)_3$), cyanic acid ($C_3H_3N_3O_3$), methanol (CH_3OH) and $AlCl_3 \cdot 6H_2O$ were all purchased from Aladdin (Shanghai, China) and used without further purification.

3.2. Preparation of Photocatalyst

First, melamine (1.5 g) and cyanic acid (1.5 g) were mixed in deionized water for 6 h at room temperature to form a supramolecular complex, cyanuric acid–melamine (CM). Then, the CM was ultrasonically dispersed in 100 mL of methanol for 30 min to obtain Part 1. $\text{AlCl}_3 \cdot 6\text{H}_2\text{O}$ was used to prepare an AlCl_3 solution (0.7 mol L^{-1} , 100 mL) and heated to $90 \text{ }^\circ\text{C}$. At the same temperature ($90 \text{ }^\circ\text{C}$), 1 g of Al-Ga-In ternary alloy was added into the solution and stirred for 3 h until the reaction was completed. It is cooled to room temperature to form a colloid, and the liquid metal (Ga-In alloy liquid metal ball) present at the bottom was sucked out. Then, after removing the unreacted metal, 100 mL of methanol was added to the colloid and stirred for 2 h to obtain Part 2. The two parts activated by methanol were mixed and stirred for 2 h. Then, they were dried in a vacuum drying oven ($80 \text{ }^\circ\text{C}$). After grinding, the dried samples were heated to $600 \text{ }^\circ\text{C}$ in an argon atmosphere in a tube furnace for 4.5 h. The final product $\text{g-C}_3\text{N}_4\text{-AlO}_x$ was obtained. In addition, the part 1 and the part 2 of the different substance quantities were synthesized and tested, and the data were presented in the supplementary material.

4. Conclusions

In this article, a new preparation strategy was proposed for amorphous aluminum oxide-modified carbon nitride with aluminum alloy as an aluminum source. The introduction of amorphous aluminum oxide confers macroporosity to the skeletons of $\text{g-C}_3\text{N}_4\text{-AlO}_x$. The material prepared by this method shows a smaller grain size, larger specific surface area, wider light response range, better photocatalytic performance and different band structure in comparison with $\text{g-C}_3\text{N}_4$. These changes help with the improvement of its photocatalytic performance.

Supplementary Materials: The following are available online at <http://www.mdpi.com/2073-4344/10/9/1036/s1>. Figure S1: XRD pattern of each synthetic sample: (a,b) before roasting and (c,d) after roasting; Figure S2: (a,c) N_2 adsorption–desorption isotherm and (b,d) pore size distribution of samples; Figure S3: TEM images of $\text{g-C}_3\text{N}_4\text{-AlO}_x$; Figure S4: FTIR absorption spectra of the samples; Figure S5: The XPS survey spectra of the samples; Figure S6: UV–vis absorption spectra of the samples; Figure S7: (a,c) photocatalytic activity comparison for RhB photodegradation by the samples under visible light irradiation, and (b,d) first order profiles of photodegradation of RhB by the samples.

Author Contributions: Formal analysis, investigation, writing—original draft, and writing—review and editing, Y.Z.; methodology and conceptualization, L.L. and C.W. (Cundi Wei); project administration, Q.A.; validation, C.W. (Congcong Wang) and W.F. All authors have read and agreed to the published version of the manuscript.

Funding: This research was funded by the Jilin University Key Laboratory of Automobile Materials of the Ministry of Education (45119031B028), the State Key laboratory of Inorganic Synthesis & Preparative Chemistry (2020-39), the National Natural Science Foundation of China (grant No. 41472035), and the Province/Jilin University co-construction project funds for new materials (SXGJSF 2017-3).

Conflicts of Interest: The authors declare no conflict of interest.

References

1. Dai, L.; Chang, D.W.; Baek, J.B.; Lu, W. Carbon nanomaterials for advanced energy conversion and storage. *Small* **2012**, *8*, 1130–1166. [[CrossRef](#)] [[PubMed](#)]
2. Jiang, Y.; Qu, F.; Tian, L.; Yang, X.; Zou, Z.; Lin, Z. Self-assembled $\text{g-C}_3\text{N}_4$ nanoarchitectures with boosted photocatalytic solar-to-hydrogen efficiency. *Appl. Surf. Sci.* **2019**, *487*, 59–67. [[CrossRef](#)]
3. Chen, Y.; Lin, B.; Wang, H.; Yang, Y.; Zhu, H.; Yu, W.; Basset, J.M. Surface modification of $\text{g-C}_3\text{N}_4$ by hydrazine: Simple way for noble-metal free hydrogen evolution catalysts. *Chem. Eng. J.* **2016**, *286*, 339–346. [[CrossRef](#)]
4. Li, F.T.; Xue, Y.B.; Li, B.; Hao, Y.J.; Wang, X.J.; Liu, R.H.; Zhao, J. Precipitation Synthesis of Mesoporous Photoactive Al_2O_3 for Constructing $\text{g-C}_3\text{N}_4$ -Based Heterojunctions with Enhanced Photocatalytic Activity. *Ind. Eng. Chem. Res.* **2014**, *53*, 19540–19549. [[CrossRef](#)]
5. Li, F.T.; Zhao, Y.; Wang, Q.; Wang, X.J.; Hao, Y.J.; Liu, R.H.; Zhao, D. Enhanced visible-light photocatalytic activity of active $\text{Al}_2\text{O}_3/\text{g-C}_3\text{N}_4$ heterojunctions synthesized via surface hydroxyl modification. *J. Hazard. Mater.* **2015**, *283*, 371–381. [[CrossRef](#)]

6. Zhang, G.; Zhang, T.; Li, B.; Jiang, S.; Zhang, X.; Hai, L.; Chen, X.; Wu, W. An ingenious strategy of preparing TiO₂/g-C₃N₄ heterojunction photocatalyst: In situ growth of TiO₂ nanocrystals on g-C₃N₄ nanosheets via impregnation-calcination method. *Appl. Surf. Sci.* **2018**, *433*, 963–974. [[CrossRef](#)]
7. Chang, F.; Zhang, J.; Xie, Y.; Chen, J.; Li, C.; Wang, J.; Luo, J.; Deng, B.; Hu, X. Fabrication, characterization, and photocatalytic performance of exfoliated g-C₃N₄-TiO₂ hybrids. *Appl. Surf. Sci.* **2014**, *311*, 574–581. [[CrossRef](#)]
8. Kamegawa, T.; Matsuura, S.; Seto, H.; Yamashita, H. A visible-light-harvesting assembly with a sulfocalixarene linker between dyes and a Pt-TiO₂ photocatalyst. *Angew. Chem. Int. Ed. Engl.* **2013**, *52*, 916–919. [[CrossRef](#)]
9. Yang, J.H.; Wang, D.G.; Han, H.X.; Li, C. Roles of Cocatalysts in Photocatalysis and Photoelectrocatalysis. *Acc. Chem. Res.* **2013**, *46*, 1900–1909. [[CrossRef](#)]
10. Cao, S.; Yu, J. g-C₃N₄-Based Photocatalysts for Hydrogen Generation. *J. Phys. Chem. Lett.* **2014**, *5*, 2101–2107. [[CrossRef](#)]
11. Wang, X.; Blechert, S.; Antonietti, M. Polymeric Graphitic Carbon Nitride for Heterogeneous Photocatalysis. *ACS Catal.* **2012**, *2*, 1596–1606. [[CrossRef](#)]
12. Butchosa, C.; Guiglion, P.; Zwiijnenburg, M.A. Carbon Nitride Photocatalysts for Water Splitting: A Computational Perspective. *J. Phys. Chem. C* **2014**, *118*, 24833–24842. [[CrossRef](#)]
13. Wang, X.; Maeda, K.; Thomas, A.; Takane, K.; Xin, G.; Carlsson, J.M.; Domen, K.; Antonietti, M. A metal-free polymeric photocatalyst for hydrogen production from water under visible light. *Nat. Mater.* **2009**, *8*, 76–80. [[CrossRef](#)] [[PubMed](#)]
14. Liu, L.; Liu, Z.; Bai, H.; Sun, D.D. Concurrent filtration and solar photocatalytic disinfection/degradation using high-performance Ag/TiO₂ nanofiber membrane. *Water Res.* **2012**, *46*, 1101–1112. [[CrossRef](#)] [[PubMed](#)]
15. Gao, Y.; Hu, M.; Mi, B. Membrane surface modification with TiO₂-graphene oxide for enhanced photocatalytic performance. *J. Membr. Sci.* **2014**, *455*, 349–356. [[CrossRef](#)]
16. Dong, F.; Zhao, Z.; Xiong, T.; Ni, Z.; Zhang, W.; Sun, Y.; Ho, W.K. In situ construction of g-C₃N₄/g-C₃N₄ metal-free heterojunction for enhanced visible-light photocatalysis. *ACS Appl. Mater. Interfaces* **2013**, *5*, 11392–11401. [[CrossRef](#)]
17. Sun, Y.F.; Cheng, H.; Gao, S.; Sun, Z.H.; Liu, Q.H.; Liu, Q.; Lei, F.C.; Yao, T.; He, J.F.; Wei, S.Q.; et al. Freestanding Tin Disulfide Single-Layers Realizing Efficient Visible-Light Water Splitting. *Angew. Chem. Int. Ed.* **2012**, *51*, 8727–8731. [[CrossRef](#)]
18. Wang, B.; Wang, Y.; Lei, Y.; Wu, N.; Gou, Y.; Han, C.; Xie, S.; Fang, D. Mesoporous silicon carbide nanofibers with in situ embedded carbon for co-catalyst free photocatalytic hydrogen production. *Nano Res.* **2016**, *9*, 886–898. [[CrossRef](#)]
19. Wang, Y.; Zeng, Y.; Li, B.; Li, A.; Yang, P.; Yang, L.; Wang, G.; Chen, J.; Wang, R. In-situ hydrothermal synthesized γ -Al₂O₃/O-g-C₃N₄ heterojunctions with enhanced visible-light photocatalytic activity in water splitting for hydrogen. *J. Energy Chem.* **2016**, *25*, 594–600. [[CrossRef](#)]
20. Lai, S.H.; Chen, Y.B.; Li, N.; Su, H.; Guo, S.H. Novel g-C₃N₄ wrapped γ -Al₂O₃ microspheres heterojunction for efficient photocatalytic application under visible light irradiation. *J. Mater. Sci. Mater. Electron.* **2017**, *29*, 4509–4516. [[CrossRef](#)]
21. Wen, J.; Xie, J.; Chen, X.; Li, X. A review on g-C₃N₄-based photocatalysts. *Appl. Surf. Sci.* **2017**, *391*, 72–123. [[CrossRef](#)]
22. Sagara, N.; Kamimura, S.; Tsubota, T.; Ohno, T. Photoelectrochemical CO₂ reduction by a p-type boron-doped g-C₃N₄ electrode under visible light. *Appl. Catal. B Environ.* **2016**, *192*, 193–198. [[CrossRef](#)]
23. Schultz, D.M.; Yoon, T.P. Solar synthesis: Prospects in visible light photocatalysis. *Science* **2014**, *343*, 1239176. [[CrossRef](#)] [[PubMed](#)]
24. Cao, S.; Low, J.; Yu, J.; Jaroniec, M. Polymeric photocatalysts based on graphitic carbon nitride. *Adv. Mater.* **2015**, *27*, 2150–2176. [[CrossRef](#)]
25. Su, F.; Mathew, S.C.; Lipner, G.; Fu, X.; Antonietti, M.; Blechert, S.; Wang, X. mpg-C₃N₄-Catalyzed Selective Oxidation of Alcohols Using O₂ and Visible Light. *J. Am. Chem. Soc.* **2010**, *132*, 16299–16301. [[CrossRef](#)]
26. Ye, C.; Li, J.X.; Li, Z.J.; Li, X.B.; Fan, X.B.; Zhang, L.P.; Chen, B.; Tung, C.-H.; Wu, L.Z. Enhanced Driving Force and Charge Separation Efficiency of Protonated g-C₃N₄ for Photocatalytic O₂ Evolution. *ACS Catal.* **2015**, *5*, 6973–6979. [[CrossRef](#)]

27. Zhang, J.; Sun, J.; Maeda, K.; Domen, K.; Liu, P.; Antonietti, M.; Fu, X.; Wang, X. Sulfur-mediated synthesis of carbon nitride: Band-gap engineering and improved functions for photocatalysis. *Energy Environ. Sci.* **2011**, *4*, 675–678. [[CrossRef](#)]
28. Chen, Y.; Bai, X. A Review on Quantum Dots Modified g-C₃N₄-Based Photocatalysts with Improved Photocatalytic Activity. *Catalysts* **2020**, *10*, 142. [[CrossRef](#)]
29. Wang, X.; Wang, G.; Chen, S.; Fan, X.; Quan, X.; Yu, H. Integration of membrane filtration and photoelectrocatalysis on g-C₃N₄/CNTs/Al₂O₃ membrane with visible-light response for enhanced water treatment. *J. Membr. Sci.* **2017**, *541*, 153–161. [[CrossRef](#)]
30. Zhang, X.S.; Hu, J.Y.; Jiang, H. Facile modification of a graphitic carbon nitride catalyst to improve its photoreactivity under visible light irradiation. *Chem. Eng. J.* **2014**, *256*, 230–237. [[CrossRef](#)]
31. Zhang, G.; Lan, Z.A.; Lin, L.; Lin, S.; Wang, X. Overall water splitting by Pt/g-C₃N₄ photocatalysts without using sacrificial agents. *Chem. Sci.* **2016**, *7*, 3062–3066. [[CrossRef](#)]
32. Li, H.; Zhang, N.; Zhao, F.; Liu, T.; Wang, Y. Facile Fabrication of a Novel Au/Phosphorus-Doped g-C₃N₄ Photocatalyst with Excellent Visible Light Photocatalytic Activity. *Catalysts* **2020**, *10*, 701. [[CrossRef](#)]
33. Min, S.; Lu, G. Enhanced Electron Transfer from the Excited Eosin Y to mpg-C₃N₄ for Highly Efficient Hydrogen Evolution under 550 nm Irradiation. *J. Phys. Chem. C* **2012**, *116*, 19644–19652. [[CrossRef](#)]
34. Goettmann, F.; Fischer, A.; Antonietti, M.; Thomas, A. Chemical synthesis of mesoporous carbon nitrides using hard templates and their use as a metal-free catalyst for Friedel-Crafts reaction of benzene. *Angew. Chem. Int. Ed. Engl.* **2006**, *45*, 4467–4471. [[CrossRef](#)] [[PubMed](#)]
35. Yang, S.; Gong, Y.; Zhang, J.; Zhan, L.; Ma, L.; Fang, Z.; Vajtai, R.; Wang, X.; Ajayan, P.M. Exfoliated graphitic carbon nitride nanosheets as efficient catalysts for hydrogen evolution under visible light. *Adv. Mater.* **2013**, *25*, 2452–2456. [[CrossRef](#)]
36. Dong, G.; Zhao, K.; Zhang, L. Carbon self-doping induced high electronic conductivity and photoreactivity of g-C₃N₄. *Chem. Commun.* **2012**, *48*, 6178–6180. [[CrossRef](#)]
37. Yan, S.C.; Li, Z.S.; Zou, Z.G. Photodegradation of rhodamine B and methyl orange over boron-doped g-C₃N₄ under visible light irradiation. *Langmuir* **2010**, *26*, 3894–3901. [[CrossRef](#)]
38. Ji, C.; Yin, S.N.; Sun, S.; Yang, S. An in situ mediator-free route to fabricate Cu₂O/g-C₃N₄ type-II heterojunctions for enhanced visible-light photocatalytic H₂ generation. *Appl. Surf. Sci.* **2018**, *434*, 1224–1231. [[CrossRef](#)]
39. Wang, H.; Bai, J.; Dai, M.; Liu, K.; Liu, Y.; Zhou, L.; Liu, F.; Liu, F.; Gao, Y.; Yan, X.; et al. Visible light activated excellent NO₂ sensing based on 2D/2D ZnO/g-C₃N₄ heterojunction composites. *Sens. Actuators B Chem.* **2020**, *304*, 127287. [[CrossRef](#)]
40. Chen, X.; Hu, S.Z.; Li, P.; Li, W.; Ma, H.F.; Lu, G. Photocatalytic Production of Hydrogen Peroxide Using g-C₃N₄ Coated MgO-Al₂O₃-Fe₂O₃ Heterojunction Catalysts Prepared by a Novel Molten Salt-Assisted Microwave Process. *Acta Phys.-Chim. Sin.* **2017**, *33*, 2532–2541.
41. Song, J.; Wang, X.; Ma, J.; Wang, X.; Wang, J.; Zhao, J. Visible-light-driven in situ inactivation of *Microcystis aeruginosa* with the use of floating g-C₃N₄ heterojunction photocatalyst: Performance, mechanisms and implications. *Appl. Catal. B Environ.* **2018**, *226*, 83–92. [[CrossRef](#)]
42. Wang, J.; Chen, J.; Wang, P.; Hou, J.; Wang, C.; Ao, Y. Robust photocatalytic hydrogen evolution over amorphous ruthenium phosphide quantum dots modified g-C₃N₄ nanosheet. *Appl. Catal. B Environ.* **2018**, *239*, 578–585. [[CrossRef](#)]
43. Lan, Y.; Li, Z.; Xie, W.; Li, D.; Yan, G.; Guo, S.; Pan, C.; Wu, J. In situ fabrication of I-doped Bi₂O₂CO₃/g-C₃N₄ heterojunctions for enhanced photodegradation activity under visible light. *J. Hazard. Mater.* **2020**, *385*, 121622. [[CrossRef](#)] [[PubMed](#)]
44. Tallapally, V.; Damma, D.; Darmakkolla, S.R. Facile synthesis of size-tunable tin arsenide nanocrystals. *Chem. Commun.* **2019**, *55*, 1560–1563. [[CrossRef](#)] [[PubMed](#)]
45. Holger, B.; Elena, V.S.; Aymeric, R.; Ivo, M.; Andreas, K.; Gerhard, G.; Horst, W. Determination of Nanocrystal Sizes: A Comparison of TEM, SAXS, and XRD Studies of Highly Monodisperse CoPt₃ Particles. *Langmuir* **2005**, *21*, 1931–1936.

